Magnesium Technology 2013
Edited by: Norbert Hort, Suveen N. Mathaudhu, Neale R. Neelameggham, and Martyn Alderman
TMS (The Minerals, Metals & Materials Society), 2013

Magnesium Technology 2013

Solidification

Magnesium Technology 2013
Edited by: Norbert Hort, Suveen N. Mathaudhu, Neale R. Neelameggham, and Martyn Alderman
TMS (The Minerals, Metals & Materials Society), 2013

COMPUTATIONAL MULTI-SCALE MODELING OF THE MICROSTRUCTURE AND SEGREGATION OF CAST Mg ALLOYS AT LOW SUPERHEAT

Laurentiu Nastac and Nagy El-Kaddah
Department of Metallurgical Engineering, University of Alabama, Tuscaloosa, Alabama 35487 USA

Keywords: Casting Mg alloys, Microstructure evolution, Stochastic mesoscopic modeling

Abstract

It is well known that casting at low superheat has a strong influence on the solidification structures of the cast alloy. Recent studies on casting magnesium AZ alloys at low superheat using the Magnetic Suspension Melting (MSM) process have shown that the cast alloy exhibit a fine globular grain structure, and the grain size depend on the cooling rate. This paper describes a stochastic mesoscopic model for predicting the grain structure and segregation in cast alloys at low superheat. This model was applied to predict the globular solidification morphology and solute redistribution of Al in cast Mg AZ31B alloy at different cooling rates. The predictions were found to be in good agreement with the observed grain structure and Al segregation. This makes the model a very useful tool for optimizing the solidification structure of cast magnesium alloys.

Introduction

It is well established that the grain size, and solute segregation and precipitation of intermetallic phases within the grain have significant influence on mechanical properties of the cast alloys [1]. For typical cooling rates of sand and die castings -- in the range of 0.1-100°C/s -- the grain structure is dendritic, with segregation of the alloying elements in the matrix between the secondary dendrite arms [2, 3]. The detrimental effect of segregation on mechanical properties is generally minimized by reducing the grain size of as-cast alloy through either grain refinement and/or casting at high cooling rates [2-4].

Much of research efforts to minimize the effects of segregation and intermetallic precipitates on the mechanical properties have been focused on grain refinement of the alloys. The addition of various grain refiners such as carbon and zirconium on the final grain structure has been extensively investigated [5-7]. These studies showed that grain refiners significantly reduce the grain size, and retain the dendritic solidification morphology of cast alloy which is generally undesirable as it cause entrapment of aluminum rich secondary-α phase between secondary dendrite arms [7,8].

Casting at low superheat is another method for grain refinement of cast alloys. This method not only reduces the grain size, but also changes the solidification morphology from a dendritic to a globular structure. The idea behind this technique is to suppress the formation of the columnar zone by reducing temperature gradient at the solidification front and to significantly reduce the growth rate to achieve plane front solidification. Casting at low superheat was successfully applied to grain refine superalloys [9-11], Al-Li 2090 and 8090 alloys [12,13] and more recently to Mg AZ31B alloy [14-16]. Superalloys studies were carried out using Microcast X process [9], while grain refinement of Al and Mg alloys was investigated using the Magnetic Suspension Melting (MSM) process [17]. The average grain size for unidirectionally-solidified Al-Li 2090 and 8090 alloys using a stainless steel bottom chill mold was about 30 μm, while that for Mg AZ31B alloy was approximately 80 μm. Increasing the cooling rate by using a copper bottom chill mold was found to further decrease the grain size of the Mg alloy [16]. These studies have also shown that segregation of secondary and intermetallic phases did not occur within the grain, but rather only at the grain boundaries.

Recently, simulation of microstructure evolution during solidification has become a powerful tool for predicting the grain structure and segregation in cast alloys. Phase Field [18], Monte Carlo [19], Cellular Automaton (CA) [19-21], Stochastic Modeling [19-22], and Voronoi Tessellation [23] are the most common methods for simulating microstructure evolution during solidification. This paper describes a stochastic globular solidification model for cast alloys at low superheat and critically examines the model by comparing theoretical predictions of grain structure and segregation of cast Mg AZ31B alloy at low superheat against experimental measurements.

The stochastic globular solidification model

This section presents the formulation for a stochastic model for globular solidification. This model is based on previously developed models for dendritic solidification [19-22]. The presented globular solidification model takes into account the nucleation and growth of hexagonal crystals.

Model formulation

A stochastic mesoscopic model for grain structure evolution includes nucleation and growth kinetics, as well as the growth anisotropy and grain selection mechanisms. The geometry of the solidified material is first enmeshed in macro-volume elements for which energy, mass, and momentum transport can be calculated by a classical deterministic methods. Then, each macro-volume is subdivided into a number of cubic micro-volume elements that have a state index associated with them. In the time-step calculation, the average temperature of the specimen is calculated from an energy balance. When the average temperature is lower than the equilibrium (or nucleation)

temperature, the nucleation and growth of grains begin. The structure of the stochastic micro-model consists of a regular network of microcells that resembles the macro-volume element.

The mesoscopic model is characterized by: (a) geometry of the microcell, (b) state of the microcell, (c) neighborhood configuration, and (d) transition rules that determine the state of the microcell. The geometry of microcell is chosen to be cubic in 3-D and square in 2-D calculations. Each microcell can have only two possible states: either liquid or solid. The ratio between the number of solid microcells and the total number of microcells represents the fraction of solid within the macro-volume element. The neighborhood configurations are based on the first- and second-order nearest neighbor microcell. The probabilistic selection of these configurations is based upon the crystallographic anisotropy of grain growth. More details about the selection of the neighborhood configurations are shown in references [19, 21]. Solidification behavior depends to a great extent on the transition rules. In the present model, the change of state of the microcell from liquid to solid is initiated either by either nucleation or growth kinetics. The models for the description of nucleation and growth kinetics in the microcells are initiated based on the local solidification start times, t_L, which are computed by interpolating the local solidification start times of the macro-volume elements.

Growth anisotropy and probabilistic selection of neighbourhood configuration

At the beginning of the simulation, all the microcells are liquid, and their state index is set to zero. As nucleation proceeds, some microcells become solid, and their index is changed to an integer larger than zero, *n*. The microcells in contact with the mold wall are identified with a different reference index, *m*. The index is transferred from the parent microcell to adjacent microcells, as they become solid through growth. For the case of dendritic solidification of AZ31B alloys, the integer takes into account the preferential growth of hexagonal crystals in the prism direction. The anisotropic characteristic in the prism direction certainly results in 6-fold preferred growth directions with angles between the primary trunks of dendrites of 60°. For graphical representation each integer has a color associated with it, and each microcell is a pixel on the computer screen. The crystallographic orientation of the new grains is chosen randomly among 255 orientation classes, which are the first 255 colors used for graphical representation.

In 2-D calculations, the probability, $dp(\theta)$, that a newly nucleated grain has a principal growth direction in the range $(\theta, \theta + d\theta)$ is given by:

$$dp(\theta) = \frac{3}{\pi} d\theta \qquad (1)$$

where $3/\pi$ takes into account the six-fold symmetry of the hexagonal crystal, *i.e.*, the integral of $dp(\theta)$ from $-\pi/6$ to $\pi/6$ is equal to unity.

Nucleation

The number of grains, δN_e, that nucleate in the volume of the liquid and at the surface of the mold during one micro-time step, δt, are calculated by using nucleation site distribution, $N_e(\delta t)$. These distributions can be calculated by assuming some experimental approaches similar to those already used in deterministic models of solidification. The instantaneous nucleation model presented in [24] was used in this work to calculate the nucleation site distribution. Other nucleation models are described in references [21, 25]. Assuming no grain movement in the liquid, the grain density at any given location, *N*, can be expressed as a function of local cooling rate:

$$\delta N_e = C_0 + C_1 \dot{T} + C_2 \dot{T}^2 \qquad (2)$$

where C_0, C_1, and C_2 are the nucleation parameters determined from experiments and $\dot{T}$ is the local cooling rate at the beginning of solidification.

The probability, dp_e, for a microcell located in the bulk of the liquid or at the surface of the mold to nucleate during the micro-time step, δt, are calculated as

$$dp_e = \frac{\delta N_e}{N^v_{\mu VE} - N^s_{\mu VE}} \qquad (3)$$

where $N^v_{\mu VE}$ and $N^s_{\mu VE}$ are the number of microcells in the bulk and at the metal-mold interface, respectively. During each time-step calculation both metal-mold interface and bulk microcells are scanned and a random number, *rand*, is generated for each of them ($0 \leq rand \leq 1$). The nucleation of a microcell that is still liquid will occur only if $rand \leq dp_e$.

Growth

It is assumed that a nucleus formed at a particular location will grow based upon a growth kinetics model and a neighborhood configuration rule previously described. As nucleation proceeds, the microcell becomes active (*n* or *m* > *0*) and can grow over a distance, $d_{\mu VE}(t)$, that is given by the following equation:

$$d_{\mu VE}(t) = \int_{t_0}^{t} V(\Delta T) dt \qquad (4)$$

where t_0 is the initial time, *t* is the actual time, and *V* is the growth velocity.

The initial time is defined as either the nucleation time, if growth is initiated through a nucleus, or the capturing time, if growth is initiated by capturing another microcell. At the capturing time, t_c, the initial microcell on which the growth was initiated captures the nearest neighbors based on a selected neighborhood configuration. For the case of

equiaxed growth, this occurs when $d_{\mu VE}(t_c)$ is equal to the distance

$$a_\theta = a\sqrt{tan^2\theta + 1} \qquad (5)$$

where a is the size of the microcell for the stochastic network and θ takes values from -π/6 to π/6. At the capturing time, the initial microcell becomes solid and its state index is transferred to the captured neighbors.

In order to reflect the probabilistic nature of grain extension, the nearest neighbors are trapped by the active microcells only when a randomly generated number, *rand*, is smaller than the capture probability, p_g, defined as follows:

$$p_g = \frac{d_{\mu VE}(t)}{a_\theta} \qquad (6)$$

Further, the same procedure is used until all microcells become solid.

The growth kinetics model presented in [19] is applied for equiaxed solidification, where the growth velocity is described by

$$V = \mu\,\Delta T^2 \qquad (7)$$

where $\mu = \frac{2\sigma^*}{\Gamma}\left[\frac{m_L(k-1)C_L^*}{D_L} + \frac{\rho L}{K_L}\right]^{-1}$

D_L is the liquid diffusivity, Γ is the Gibbs-Thomson coefficient, k is the partition ratio, m_L is the liquidus slope, ρ is the density, L is the latent heat of fusion, K_L is the liquid thermal conductivity, C_L^* is the liquid interface concentration, and the stability constant $\sigma^* = 1/4\pi^2$.

The melt undercooling for the system under consideration can be calculated based on the following definition/assumption:

$$\Delta T = T_L + m_L\left(C_L^* - C_o\right) - T_b \qquad (8)$$

where T_L is the equilibrium liquidus temperature, $\langle C_L \rangle^L$ is the intrinsic volume-averaged liquid concentration, and T_b is the bulk temperature defined as the average temperature in the volume element, C_L^* , is calculated with the segregation model described in [19, 22].

Comparison of the simulated and observed structure of cast Mg AZ31B

In this section, we shall provide a critical assessment of the stochastic model by comparing the theoretically predicted grain size and Al segregation of cast Mg AZ31B alloy at low superheat against experimental measurements at two different cooling rates. The cast Mg alloy was prepared using the MSM process, which is capable of casting metal at superheat as low as 5°C. Casting of the metal was carried out in bottom-chilled mold shown in Figure 1. The mold was made of a ceramic tube with a metal block in the bottom. A battery of thermocouples was used to measure the cooling rates along the ingot. In this work, stainless steel and copper chill blocks were used to investigate the effect of solidification rate on cast structure. The details of the experimental MSM system and operating conditions are available in [14 - 16].

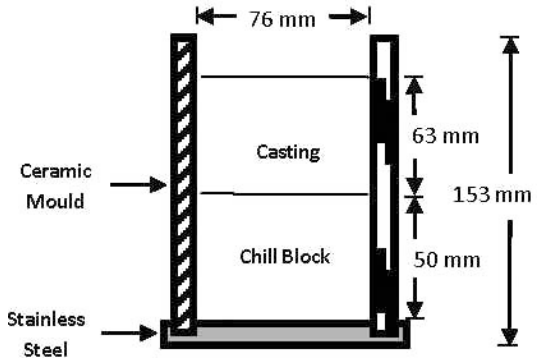

Fig 1. Sketch of the casting mold

The simulation of the microstructure in the bottom-chill mold shown in figure 1 was carried out assuming zero heat flux at the top and side walls. In these computations, the pouring temperature of the Mg alloy was 635°C and the initial temperature of the chill block was 20°C. Table 1 presents the data used in the microstructure modeling of Mg AZ31B alloy.

Table 1. Data Used in Microstructure Modeling of AZ31B

Solidification Kinetics Property	AZ31B
Liquid diffusivity, D_L [$m^2\ s^{-1}$]	$3x10^{-9}$
Solid diffusivity, D_S [$m^2\ s^{-1}$]	$1x10^{-12}$
Liquidus slope [K wt. $\%^{-1}$] [14]	m_L = -6.6
Initial Al concentration [wt. %]	C_o = 3.14
Al partition coefficient [14]	k = 0.39
Eutectic [wt. %]	32.3
Gibbs-Thomson coefficient, G [K m]	0.9×10^{-7}
Equiaxed nucleation parameters dN_e [nuclei m^{-3}]	$C_0 = 5x10^{12}$; $C_1 = 1x10^{12}$; $C_2 = 0$

Figure 2 shows the measured cooling curves of the cast alloy in the mold for copper and stainless steel chill blocks. This figure shows that the cooling rate of the Mg alloy in the copper chill mold is much faster than that in the stainless steel chill mold. The Initial cooling rate in the copper chill mold is about 2°C/s, while it is 1°C/s for stainless steel chill mold. Figure 3 shows an expanded view of the cooling curves within the solidification range. As seen in this figure, the experimental solidification times for copper and stainless steel chill blocks were found to be 24.7s and 36.1s, respectively. Here it should be mentioned that these solidification times were in reasonable agreement with model predictions.

Figures 4 and 5 show a comparison between the theoretically predicted and experimentally measured grain structure of cast Mg AZ31B alloy for low and high cooling rates, respectively. As seen in these figures, the model reasonably predicts the mean grain size and size distribution over the range of the cooling rate investigated. It also qualitatively predicts the expected decrease of the grain size with increasing the cooling rate.

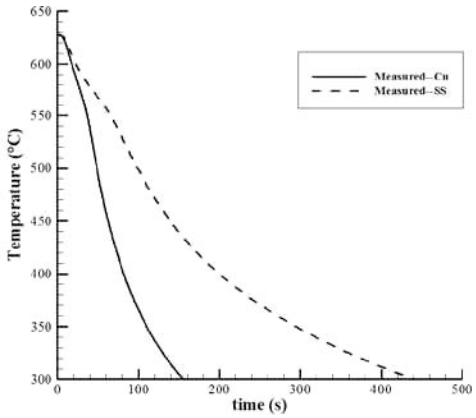

Fig 2. Cooling curves for copper and stainless steel chill blocks

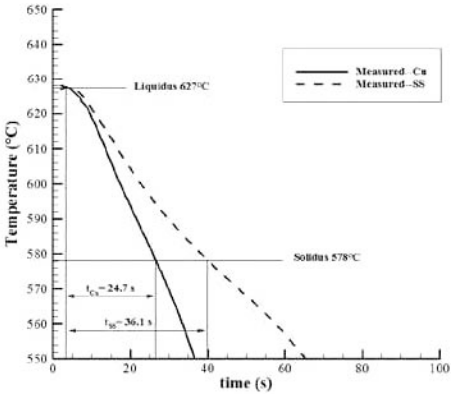

Fig 3. Cooling curves for solidification region.

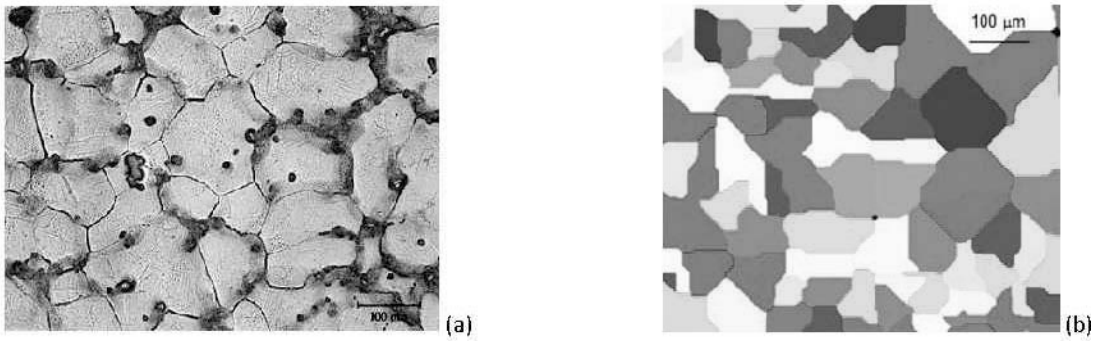

Fig 4. Comparison between (a) experimental and (b) simulated grain structure for stainless steel bottom chill mold

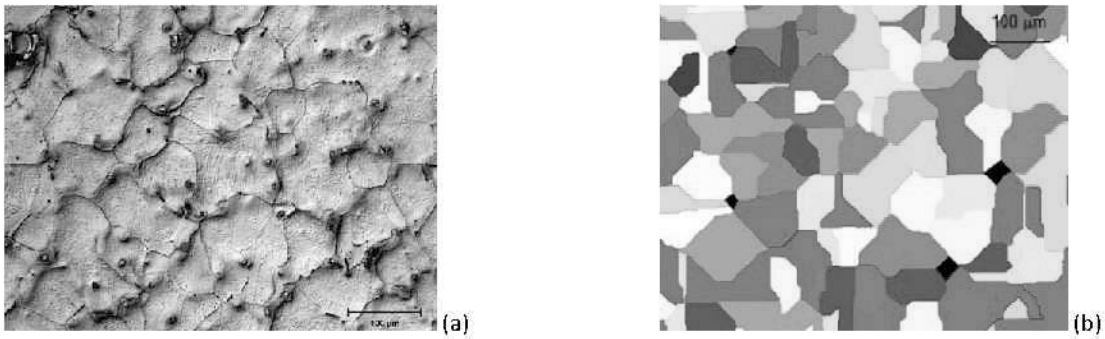

Fig 5. Comparison between (a) experimental and (b) simulated grain structure for stainless steel bottom chill mold

Figure 6 shows the EDS maps of Al segregation for the two cooling rates investigated. The light areas correspond to Al-rich secondary-α phase, while the more bright spots are the $Mg_{17}Al_{12}$ intermetallic. These phases are essentially found at the grain boundaries, thus confirming globular solidification morphology. These figures also show that the concentration of aluminum in the matrix is much lower than that at the grain boundaries, and the cooling rate has little effect on concentration profile across the grain. The measured and predicted Al segregation profile at the end of solidification within 2 globular grains is illustrated in figure 7. The excellent agreement between the measured and predicted magnitude and profile of Al distribution validates the segregation formulation of the model for globular solidification.

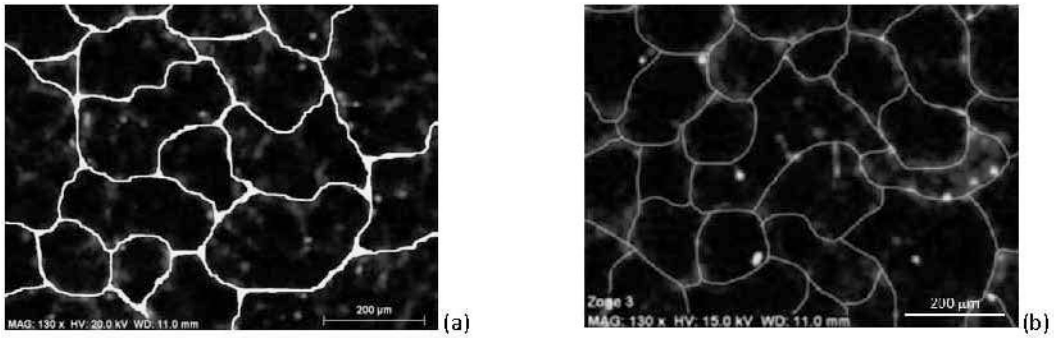

Fig 6. EDS Maps of Al solute distribution in MSM cast Mg AZ31B at 8°C superheat for (a) stainless steel and (b) copper chill block

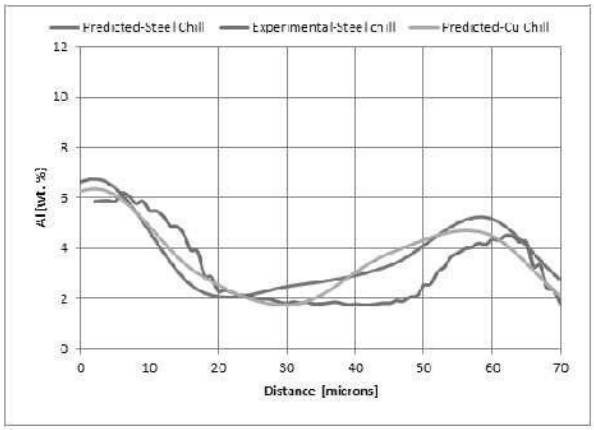

Fig 7 Comparison between the experimentally measured and theoretically predicted Al distribution across the grain

Conclusions

A stochastic mesoscopic model was developed to predict the microstructure evolution in Mg AZ31B castings. The model predictions were found to be in good agreement with the experimental measurements in terms of the microsegregation and the average grain size of the cast alloy. This suggests that the developed stochastic mesoscopic model can be used to assist in controlling the microstructure of cast alloys with globular morphologies.

Acknowledgment

The authors graciously thank the National Science Foundation for funding this investigation under Grant number CMMI-0856320.

References

1. N. Li, R. Osborne, B. Cox, B., and D. Penrod, "Magnesium Engine Cradle: The USCAR Structure Cast Magnesium Development Project: ASE paper," 337 (2005).
2. J.P. Thomson, S. Xu, M. Sadayappan, P.D. Newcombe, L. Millette, and M. Sahoo, "Low Pressure Casting of Magnesium Alloys AZ91 and AM50," AFS Transactions, 1-10 (2004).
3. S.G. Lee, G.R. Patel, and A.M. Gokhale, "Characterization of the effects of process parameters on macrosegregation in a high-pressure die-cast Magnesium alloy," Materials Characterization, 55, 219-224 (2005).
4. Y. Chino, T. Furuta, M. Hakamada, and M. Mabuchi, "Influence of distribution of oxide contaminants on fatigue behavior in AZ31 Mg alloy recycled by solid-state processing," Materials Science and Engineering: A, 424, 355-360 (2006).
5. D. H. StJohn, M. Qian, M. A. Easton, and P. Cao, Native Grain Refinement of Magnesium Alloys: Scripta Materialia 53 (2005) 841-844.
6. P. Cao, M. Qian, and D. H. StJohn, "Effect of iron on grain refinement of high-purity Mg–Al alloys," Scripta Materialia, V51 (2004) p.125-129

7. G. Han, X. Liu, and H. Ding, "Grain refinement of AZ31 magnesium alloy by new Al-Ti-C master alloys," Transactions of Nonferrous Metals Society of China, V19 (2009) p.1057-1064
8. D.G. Leo Prakash, Doris Regener, "Quantitative characterization of $Mg_{17}Al_{12}$ phase and grain size in HPDC AZ91 Magnesium Alloy," Journal of Alloys and Compounds, V461 (2007) p. 139-146
9. J.R. Brinegar, *et al.*, U.S. patent, No. 4832112 (1989).
10. Y. Ma, et al., Journal of Materials Processing Technology 137, (2003) p 35–39.
11. L. Liu, *et al.*, Materials Science and Engineering A 394 (2005) p1–8.
12. J. Reynolds, M. Shamsuzzoha and N. El-Kaddah, Characterization of Al-Li Castings Produced by the Magnetic Suspension Melting Process: in "Proceedings of the 4th Decennial International Conference on Solidification Processing", edited by J. Beech and H. Jones (Department of Engineering Materials, University of Sheffield, Sheffield, 1997) p. 45-48.
13. C. Mahato, M. Shamsuzzoha and N. El-Kaddah, Solidification Morphology and Structure of Cast Al-Li 2090 Alloy at Low Superheats: in "Solidification of Aluminum Alloys", edited by M. G. Chu, D. A. Granger and Q. Han (TMS, Warrendale, OH, 2004) p. 321-328.
14. N. Rimkus, L. Vihtelic, and N. El-Kaddah, "Grain and Microstructure of Cast Mg AZ31-B Alloy Produced by the Magnetic Suspension Melting Process," *Proceedings of* Light Weight Materials for Vehicles and Components Symposium, (TMS, Warrendale, OH, 2010) p.753-761.
15. N. Rimkus, M.L. Weaver, and N. El-Kaddah, "Microstructure and Mechanical Behavior of Cast Mg AZ31B Alloy Produced by the Magnetic Suspension Melting Process," *Proceedings of Magnesium Technology 2011,* (TMS, Warrendale, OH, 2011) p. 335-343.
16. G. Poole, N. Rimkus, A. Murphy, P. Boehmcke, and N. El-Kaddah, "Effect of Solidification Rate on Microstructure of Cast Mg Alloys at Low Superheat," *Proceedings of Magnesium Technology 2012*, (TMS, Warrendale, OH, 2012) p. 161-164.
17. N. El-Kaddah, T.S. Piwonka, and J.T. Berry, U.S. patent, No. 5033948 (1991).
18. J.A. Warren, and W.J. Boettinger, *Acta Materialia*, **43** 2 (1995) p. 689.
19. L. Nastac, *Modeling and Simulation of Microstructure Evolution in Solidifying Alloys* Springer-New York (2004): http://www.springer.com/materials/special+types/book/978-1-4020-7831-6
20. D.M. Stefanescu, *Science and Engineering of Casting Solidification* Springer (2002) p. 145-148.
21. L. Nastac, and D.M. Stefanescu, *Modelling and Simulation in Materials Science and Engineering* **5** (1997) p. 391-420.
22. L. Nastac, *Acta Materialia* **17** (1999) p. 4253.
23. S. Vernede, and M. Rappaz, *Acta Materialia* **55** (2007) p.1703.
24. D.M. Stefanescu, G. Upadhya, and D. Bandyopadhyay, "Heat Transfer-Solidification Kinetics Modeling of Solidification of Castings", *Metallurgical and Materials Trans. A* **21** (1990) p 997.
25. W. Olfield, "A Quantitative Approach to Casting Solidification: Freezing of Cast Iron", *ASM Trans.* **59** (1996) p 945.